PNAS

Supplementary Information for

Robust acoustic trapping and perturbation of single-cell microswimmers illuminate three-dimensional swimming and ciliary coordination

Mingyang Cui,[1,2] Susan K. Dutcher,[3] Philip V. Bayly,[1] and J. Mark Meacham[1,*]

[1] Department of Mechanical Engineering and Materials Science, Washington University in St. Louis, St. Louis, Missouri 63130, USA
[2] Research Laboratory of Electronics, Massachusetts Institute of Technology, Cambridge, Massachusetts 02139, USA
[3] Department of Genetics, Washington University School of Medicine in St. Louis, St. Louis, Missouri 63110, USA

[*] J. Mark Meacham, Jubel Hall Rm 203K, Department of Mechanical Engineering and Materials Science, Washington University in St. Louis, 1 Brookings Dr., St. Louis, Missouri 63130, USA, (314) 935-3821, meachamjm@wustl.edu

This PDF file includes:

> Supplementary text
> Figures S1 to S4 (not allowed for Brief Reports)
> Table S1 (not allowed for Brief Reports)
> Legends for Movies S1 to S9
> SI References

Other supplementary materials for this manuscript include the following:

> Movies S1 to S9

Acoustic field-microswimmer interactions

Acoustic microfluidic devices typically operate using bulk acoustic waves (BAW) excited by a piezoelectric element or surface acoustic waves (SAW) traveling on a piezoelectric substrate. When the actuator is driven harmonically, time-harmonic oscillating pressure and velocity fields develop inside the fluidic domain of the assembly. The first-order acoustic fields drive two second-order phenomena that influence the motion of suspended cells. Acoustic streaming arises from the viscous attenuation of the acoustic waves, resulting in a steady fluid flow that induces a drag force F^{drag} on the cells. The acoustic radiation force F^{rad} is generated as acoustic waves scatter on the cells, which moves the cells to acoustic radiation force potential minima (i.e., to acoustic pressure minima for *C. reinhardtii* cells that have a positive acoustic contrast factor) [1]. Because these two forces scale differently with particle radius a ($F^{\text{drag}} \propto a$ and $F^{\text{rad}} \propto a^3$), the motion of micrometer-sized particles (e.g., mammalian cells, yeast, or microbeads) is typically dominated by the acoustic radiation force, while the motion of submicrometer-sized particles (e.g., bacteria, biomolecules, and viruses) is dominated by the drag force due to acoustic streaming for MHz-frequency ultrasound. The size of the *C. reinhardtii* cell body (~8 µm) is much larger than the critical particle diameter delineating streaming versus acoustic radiation force dominated motion, while the cross-section of the cilia (~200 nm) is much smaller [2]. Thus, exposure to the acoustic field has a negligible effect on the ciliary waveform, and the motion of a swimming *C. reinhardtii* cell is governed by the following force balance

$$\frac{4\pi}{3} a^3 \rho_c \partial_t \boldsymbol{u} = \boldsymbol{F}^{\text{rad}} + \boldsymbol{F}^{\text{drag}} + \boldsymbol{F}^{\text{swim}},$$

where a, ρ_c, and $\boldsymbol{u}$ are the radius of the cell, density, and cell velocity (net velocity); $\boldsymbol{F}^{\text{rad}}$, $\boldsymbol{F}^{\text{drag}}$, and $\boldsymbol{F}^{\text{swim}}$ are the acoustic radiation force, viscous drag force, and intrinsic swimming force of the cell. Considering *C. reinhardtii* is a nearly spherical particle and neglecting wall effects, the primary acoustic radiation force on a *C. reinhardtii* cell is described as

$$\boldsymbol{F}^{\text{rad}} = -\frac{4\pi}{3} a^3 \nabla \left[f_0 \frac{1}{2} \kappa_o \langle p_{\text{in}}^2 \rangle - f_1 \frac{3}{4} \rho_o \langle v_{\text{in}}^2 \rangle \right],$$

where

$$f_0 = 1 - \tilde{\kappa} \text{ and } f_1 = \frac{2(\tilde{\rho} - 1)}{2\tilde{\rho} + 1}.$$

Here p_{in} and v_{in} are the incoming acoustic pressure and velocity fields at the cell location, and $\langle \rangle$ represents time averaging over a full oscillation period of a time-harmonic quantity [3, 4]. f_0 and f_1 are dimensionless functions of the ratios of particle/fluid compressibility and density, $\tilde{\kappa} = \kappa_p/\kappa_o$ and $\tilde{\rho} = \rho_p/\rho_o$, respectively. The acoustic contrast factor is expressed as

$$\Phi = \frac{1}{3} f_0 + \frac{1}{2} f_1.$$

In this equation, f_0 and f_1 determine the sign of Φ (toward the pressure nodes if Φ is positive or toward the pressure antinodes if Φ is negative). The Stokes drag force is represented by

$$\boldsymbol{F}^{\text{drag}} = -6\pi a \eta \boldsymbol{u}.$$

Here, η is the dynamic viscosity of the fluid. Similarly, the self-propulsive swimming force of a biciliated *C. reinhardtii* cell can be written as

$$\boldsymbol{F}^{\text{swim}} = 6\pi a \eta \boldsymbol{u}^{\text{swim}}$$

where u^{swim} is the swimming velocity of a free-swimming cell. From these equations, we see that to achieve zero velocity, i.e., to trap a swimming *C. reinhardtii* cell, a high acoustic radiation force is needed to overcome the self-propulsive swimming force.

Cilia dynamics theory

We have previously described the kinematic analysis of *C. reinhardtii* cilia in detail [5-7]. High resolution videos were analyzed using custom-made programs written in MATLAB. The process is briefly summarized here. First, the motion of a cilium was described with respect to a body-fixed reference Cartesian frame using a digital image registration process. Then, positions of points on the cilium were extracted from the video and manually traced. These cilium positions over time were input to an automated fourth-order polynomial curve fitting algorithm that provided a quantitative description of the cilium in both space and time. Next, an average characteristic beat was calculated for the regularly beating cilium. To describe the ciliary waveform during nonperiodic beating, the characteristic beat was computed and analyzed transiently to identify periods of synchronous and asynchronous beating, which were evaluated separately. Finally, waveform kinematic parameters, forces, and torques were calculated.

Analysis of cell body motion. Raw video with a defined region of interest (ROI) was preprocessed in MATLAB. Note that for most cases at least five in-plane beating cycles fell within the duration of video frames being analyzed (120–200 frames captured at 2000 fps for ~1 cP and 3 cP cases, depending on temperature; 200–300 frames captured at 1000 fps and 500 fps for 5 cP and 8 cP cases, respectively). Due to the significantly reduced beat frequency when cells were suspended in the highest viscosity fluids, *cis* cilium beating for η = 8 cP included only at least two complete beats. Each frame of the analyzed video was compared to the first image in a sequence to define the rotation angles and displacements of the cell body. All cell body rotations were analyzed in a counterclockwise progression, i.e., video frames were flipped to reverse the direction of rotation if a particular cell was found to rotate clockwise for consistency.

Cilium position description. The cilium was manually traced, followed by automatic curve fitting to describe the cilium position in space and time. After adjustment of image contrast and correction of body orientation, video was cropped to define the ROI for manual tracing. This also required that the proximal end of the cilium (base) be identified by the user. For each frame of the video, the cilium was traced using the ImageJ brush tool (1-px width, cyan color) on a touchscreen laptop with a digital pen (Microsoft Surface Pro 4). Then the video was saved in the AVI format and reuploaded to MATLAB. A cloud of traced points for every frame was stored as a three-dimensional (3D) array in Cartesian coordinates. Fourth-order polynomials were used to fit the points as we have described previously [7].

Characteristic average beat. The MATLAB function xcov was used to calculate an autocovariance function $\gamma(s,\tau)$ for the waveform angle $\theta_c(s,t)$ at each spatial location s along the cilium, where t is time, and τ is the time lag in autocovariance of θ_c. An aggregate autocovariance function for the cilium $\gamma_c(\tau)$ was then computed by averaging γ over s. The average peak of the autocovariance at nonzero time lag $\hat{\gamma}_c$ was used as a marker of periodicity and also to determine the period of ciliary beating. Finally, the period was used to estimate the beat frequency f_c. A theoretical value of 1.0 for $\hat{\gamma}_c$ represents perfect periodicity, meaning the covariance traces are entirely superimposed on each other; however, typical values of ~0.8 were considered to be periodic for our analysis. Less periodic motions, such as beating of the *trans* cilium during "slip" motion, had smaller values of ~0.5. If the value of $\hat{\gamma}_c$ was smaller than ~0.15, the beating of the cilium was considered to be nonperiodic [5]. For cilia that beat periodically, the beating angles θ_c were averaged together to reconstruct a characteristic beat. The waveform parameters were then calculated using this reconstructed average beat. For consistency, Cartesian coordinates were defined for the analysis of uniciliated cells such that the base of the cilium was at (0,0) and the x-axis corresponded to the direction of forward swimming for biciliated cells.

Waveform parameters and local forces. The ciliary angle $\theta_c(s,t)$ over space and time was used to extract key kinematic parameters of the beating cilium, including the average curvature $\bar{\kappa}_c$ (rad/μm) [$\kappa_c = \partial\theta_c/\partial s$; $\bar{\kappa}_c$ = mean(κ_c)] and the bend amplitude θ_c^{SD} = std(θ_c) (rad). The average and

3

standard deviation (std) were calculated over both space and time. Ciliary propulsive forces were estimated from the ciliary waveform using resistive force theory [8-10]. The normal and tangential components of the force per unit length applied by the cilium on the fluid are expressed as

$$f_N = c_N v_N \text{ and } f_T = c_T v_T.$$

Here, we used previously obtained estimates of the normal and tangential resistive force coefficients (c_N = 0.0015 pN-s/µm^2 and c_T = 0.0007 pN-s/µm^2) [6]; v_N and v_T are the normal and tangential velocity of any point on the cilium with respect to the body-fixed frame. The components of the net force applied on the cell body by a cilium F_{cx} and F_{cy} can be obtained by integrating the values of the local resistive forces in both the x- and y-directions, respectively,

$$F_{cx} = \int_0^L f_x \, ds \text{ and } F_{cy} = \int_0^L f_y \, ds,$$

where F_{cx} corresponds to the ciliary force along the swimming direction for biciliated cells. For uniciliated cells, the torque applied to the cell body by the cilium is calculated as

$$M_c = \int_0^L \left(f_y r_{cx} - f_x r_{cy} \right) ds.$$

Here, r_c is the relative position of each point on the cilium with respect to the center of the cell body. For uniciliated cells, the force exerted by the cilium is balanced by the viscous drag on the cell body after neglecting inertia in the low Reynolds number regime. Thus, the viscous force F_b and torque M_b on the cell body can be directly estimated from the cell body motion

$$F_{bx} = 6\pi\eta a_e v_{bx} \times C_{f1},$$
$$F_{by} = 6\pi\eta a_e v_{by} \times C_{f2}, \text{ and}$$
$$M_b = 8\pi\eta a_e b_e^2 \omega \times C_{f3},$$

where

$$C_{f1} = \frac{8}{3} e^3 \left[-2e + \left(1 + e^2\right) \ln \frac{1+e}{1-e} \right]^{-1},$$
$$C_{f2} = \frac{16}{3} e^3 \left[2e + \left(3e^2 - 1\right) \ln \frac{1+e}{1-e} \right]^{-1}, \text{ and}$$
$$C_{f3} = \frac{4}{3} e^3 \left(\frac{2 - e^2}{1 - e^2} \right) \left[-2e + \left(1 + e^2\right) \ln \frac{1+e}{1-e} \right]^{-1},$$

and where

$$e = \sqrt{1 - b_e^2 / a_e^2}.$$

Here, a_e, b_e, and e corresponded to the major axis, minor axis, and eccentricity of the slightly ellipsoidal cell body, v_b the velocity of body translation, and ω the instantaneous angular velocity of body rotation [6, 11].

Device fabrication

Fabrication of interdigitated transducers. The interdigitated transducer (IDT) fabrication process is illustrated in Figure S1. Two types of hybrid BAW\SAW devices were used in this work: cell population patterning devices and single-cell microswimmer trapping devices. Both types utilized

standard straight IDTs patterned on 500-μm thick, 128° Y-cut, X-propagating lithium niobate (LiNbO$_3$) substrates and wet-etched microfluidic channels in glass superstrates. The IDT fabrication process for each device type was the same. The pattern for a pair of IDTs oriented perpendicular to the x-axis of the LiNbO$_3$ was prescribed in photoresist (PR) using a laser writer (DWL66+, Heidelberg). A double layer of metal (Cr/Au, 10 nm/80 nm) was deposited over the pattern using a thermal evaporator (306 Vacuum Coater, Edwards), and standard lift off of unwanted metal over PR using acetone in a sonication bath completed the process. The widths of electrode fingers and interelectrode spacings were 140 μm, 120 μm, 100 μm, and 50 μm, respectively, for operation at ~6.6 MHz (560 μm SAW wavelength), ~8.1 MHz (480 μm), ~9.6 MHz (400 μm), and ~19.4 MHz (200 μm). The ~6.6 MHz, ~8.1 MHz, and ~9.6 MHz devices had 25 pairs of electrodes, while the 19.4 MHz devices had 40 pairs. The LiNbO$_3$ wafer was cut to size using a dicing saw (DAD 323, Disco). For the single-cell microswimmer trapping device with thin glass superstrate, inlet and outlet holes were manually drilled through the LiNbO$_3$ substrate using a 1-mm diameter diamond drill bit on a high-speed micromotor (Espert 500, Nakanishi Co.) at 20,000 rpm. The aperture of all IDTs was 7 mm, and the distance between opposing IDTs was 7.92 mm. Although ohmic heating of the IDTs may occur with such thin metal layers, the impedance was measured to be ~45 Ω, ~40 Ω, ~50 Ω, and ~75 Ω for ~6.6 MHz, ~8.1 MHz, ~9.6 MHz and ~19.4 MHz devices, respectively. The overall drive power ranged from 12–300 mW throughout the reported work. Heating of the IDTs was minimal as the impedance was below 100 Ω for all resonances. A temperature-controlled stage maintained the setpoint temperature (see below).

Fabrication of glass channels. All glass channels had a depth of ~30 μm restricting the *C. reinhardtii* cells to quasi-2D motion within the focal plane of observation [5, 12]. The side length of square chambers and the diameter of circular chambers were 545 μm for ~6.6 MHz, ~8.1 MHz, and ~9.6 MHz devices, and 275 μm for ~19.4 MHz devices, respectively. Two types of glass superstrates were prepared using different methods as shown in Fig. S1b,c. For cell population patterning, glass channels were fabricated in a 1.5-mm thick soda lime/Cr photomask blank precoated with photoresist (PR) AZ1500K (5300 Å AZ1500, Telic Co.). Chambers were isotropically wet etched to the ~30 μm depth using 48% hydrofluoric acid: 69% nitric acid: deionized (DI) water at a ratio of 2:1:8, as described previously [13], followed by photoresist and chromium removal. Inlet and outlet holes were manually drilled in the glass superstrate as described above. The single-cell microswimmer trapping glass channels were fabricated using ~170-μm thick coverslips (No. 48393, VWR international). In order to protect the glass during wet etching, the coverslips were first coated with thick metal layers (Cr/Au, 40 nm/400 nm) deposited on both sides using the thermal evaporator. In addition, PR (AZ P4620, MicroChem) was spin coated on both sides of the coverslips. The coverslips were then exposed to UV light through a prepatterned photomask (DWL66+, Heidelberg) with the microfluidic channel pattern using a mask aligner (UV-KUB 3, Kloe), followed by standard development process, wet etching, and PR and Cr/Au removal. Special attention was taken during processing of thin glass channels due to the superstrate brittleness. Both thick and thin glass channel superstrates were finally diced into 20 mm × 5 mm pieces using a dicing saw.

Device assembly. An ~5-μm thick SU-8 (SU-8 2005, MicroChem) layer was spin coated onto the IDT-patterned LiNbO$_3$ substrates as an adhesive layer. The substrates were then prebaked on a hotplate at 90°C for 75 s to solidify the SU-8, preventing excessive leakage into the channels during assembly. The channels were carefully aligned to the IDTs, and devices were returned to the hotplate at 95°C for another 45 s. At the same time, the superstrate was gently pressed against the substrate using tweezers to facilitate bonding while avoiding SU-8 leakage into the channel. The prebonded devices were exposed to UV through a prepatterned photomask to fix the adhesive bond, followed by removal of excess SU-8. The devices were ready to test after connecting electrodes using conductive silver epoxy (8331D, MG Chemicals).

Cell culture and sample preparation

C. reinhardtii cells were obtained from the Dutcher Lab at Washington University in St. Louis. Cells were cultured on agar plates under constant room lighting at 25°C for 48 hours, following a previously reported protocol [14]. Before running an experiment, cells were resuspended for 3 hrs in a test tube containing medium that lacked nitrogen (adapted from Medium I of Sager and

5

Granick) to promote gametogenesis [15]. The tube was then gently vortexed to obtain a uniform suspension of cells. To maintain cell viability during resuspension, tubes containing cell suspensions were continuously rotated at 10 rpm using a rotator (Rotator Genie SI-2110, Scientific Industries). Typical cell concentrations were 5–6 million cells per mL. Note that *C. reinhardtii* cells prefer environments between 20°C and 32°C; cell function and/or viability are compromised at temperatures exceeding 37–43°C depending on cell growth conditions [16, 17].

The viscosity of the cell suspensions was adjusted as needed by adding an appropriate volume of Ficoll 400, yielding samples with the following viscosities: 8 cP (~12% w/v Ficoll 400), 5 cP (~8% w/v Ficoll 400), and 3 cP (~5% w/v Ficoll 400). We generated these concentrations by dilution of 20% w/v Ficoll 400 solution (Sigma Aldrich). Viscosity was confirmed by rheometer (AR-G2, TA Instruments). While a slight shear thinning behavior has been reported at a very high concentration of Ficoll (52.7%) [18], the highest concentration used in our work (12%) falls in the Newtonian regime, and so the fluid was considered to be Newtonian.

The colorectal cancer line SW620 cells were obtained from the Fields Lab at Washington University in St. Louis. The SW620 cells were purchased from ATCC and cultured in RPMI medium (RPMI-1640 Medium, Sigma-Aldrich) with 10% fetal bovine serum (FBS) and antibiotics. The cell line was maintained in an incubator (HERAcell 150i CO_2 incubator, Thermo Scientific) at a temperature of 37°C and 5% CO_2. Before each experiment, cells were detached from the surface of a culture flask using a 0.05% trypsin solution (Trypsin-EDTA, Gibco). The culture flask was then loaded with cell culture medium to stop the digestion process. Cell suspensions were transferred to a test tube and centrifuged at 1260 rpm to remove the supernatant containing the staining solution. Finally, cells were resuspended in cell culture medium to the desired loading concentration. The 10 μm polystyrene (PS) beads (Sigma-Aldrich) were diluted using phosphate-buffered saline (PBS) to the desired loading concentration of 5 million per mL before each experiment.

Experimental setup and imaging approach

Optimization of operating frequency. A function generator (33522A, Agilent) and amplifier 125A250, Amplifier Research) were used to drive the hybrid BAW/SAW devices. The impedance response was determined using a PC oscilloscope (PicoScope 5444D, Pico Technology) to measure the applied voltage waveform (using a voltage probe at the piezoelectric element), the current waveform (voltage probe across a ground-side current sensing resistor), and phase (relationship between the two waveforms) over a frequency range that included the predicted operating frequency. The reflection coefficient was used to predetermine the nominal operating frequency range. *C. reinhardtii* cells were then loaded into the microfluidic channels, and the frequency corresponding to maximum nodal confinement of the cells was identified as the optimal BAW resonance for patterning and trapping cells. The experiments were conducted on a custom temperature-controlled stage (20°C unless noted; PE100, Linkam). Each population patterning and cell trapping experiment was repeated at least three times.

Imaging patterns of cell populations. The cell population patterns were visualized on the stage of an inverted microscope (Axio Observer z.1, Zeiss) using either a 10X objective (EC Plan-Neofluar 10x/0.3, Zeiss) or a 20X objective (LD Plan-Neofluar 20x/0.4 Korr, Zeiss). Videos were recorded at 32 fps at 1936 × 1460-pixel resolution (0.454 μm × 0.454 μm per pixel for 10X objective; 0.222 μm × 0.222 μm per pixel for 20X objective), using a 3-Megapixel camera and imaging software (Axiocam 503; ZEN software, Zeiss). Prior to loading samples into the microfluidic channels/chambers, the channels were flushed with isopropyl alcohol to avoid air bubble inclusion, followed by pretreatment with 3% (w/v) bovine serum albumin (BSA) (Sigma-Aldrich) in PBS for 10 min to minimize adhesion of cells to the channel walls. A custom Python program was used to precisely control experimental parameters.

Single-cell microswimmer trapping and cilia imaging. The single cell trapping experiments were imaged using phase-contrast microscopy with a 100X oil-immersion objective (EC Plan-Neofluar 100X/1.3 oil, Zeiss). Videos were recorded using a high-speed camera (FASTCAM Mini AX 200, 32GB, Photron) at 2000 fps with a pixel resolution of 0.194 μm × 0.194 μm. Frames displaying typical beating were extracted and saved in uncompressed AVI format at 30 fps. The temperature variation experiments were performed by adjusting the temperature-controlled stage

to 15°C, 20°C and 25°C. Two aluminum pieces (20 mm × 20 mm × 1.5 mm) were sandwiched between the device and stage to enhance heat conduction and temperature control. Without this addition, the ciliary beat frequency would increase by up to ~50% after only a brief actuation. The viscosity of the cell medium was varied by adding an appropriate volume of Ficoll 400 solution (Sigma Aldrich). The desired viscosity was confirmed using a rheometer (AR-G2, TA Instruments). Perturbation experiments were performed using a custom Python program to precisely control the experimental inputs.

Effect of ultrasound exposure on cilia beating

We used the uniciliate mutant strain *uni1* to quantify how ultrasound exposure affects cilia beating (n = 30). The drive frequency was 9.6 MHz with an input power of 256 mW, consistent with the operating conditions for trapping biciliate wild type cells. Cilium motion was analyzed before and during acoustic trapping. The resulting kinematic parameters are shown in Fig. S2. The cilia beat frequency f_c for acoustically confined *uni1* was only ~3 Hz higher than that measured before acoustic actuation; however, no significant difference in bend amplitude or curvature was observed.

Without acoustic actuation, f_c = 64 Hz (mean ± SD: 64.0 ± 9.1 Hz). While in the acoustic trap, the beat frequency increased to 67 Hz (67.2 ± 10.6 Hz). The observed difference between these two frequencies was significant (p<0.01), suggesting that the ultrasound accelerated the beat frequency by ~4.7%. The bend amplitude θ_c^{SD} for *uni1* cilia without and with acoustics had similar values of 0.82 rad (0.82 ± 0.06 rad) and 0.81 rad (0.81 ± 0.07 rad), respectively. In addition, the curvature $\bar{\kappa}_c$ was unchanged with identical values of -0.20 rad/μm (with acoustics -0.20± 0.03 rad/μm; without -0.20 ± 0.03 rad/μm). There was no significant difference between actuation and no actuation measurements for either amplitude or curvature. Note that although the ciliary beat frequency was slightly elevated without detectable change in waveform, this increase was due to a small increase in operating temperature (~1°C).

Effects of long-term acoustic trapping on cilia dynamics

We further investigated whether long-term exposure to ultrasound affects the ciliary beat of *uni1*. The temperature-controlled stage was set at 15°C, 20°C, and 25°C for a range of experiments. A sample size of six was used for all cases. Cell motion was recorded for 1 min under acoustic actuation, and the ciliary waveform was analyzed at 10 s intervals. The results are summarized in Fig. S3. Beat frequency f_c was slightly elevated for cells confined in the acoustic field. At 15°C and 20°C, f_c increased over the first 10 s before stabilizing. The 25°C case had a similar trend, though stabilization occurred at 20 s. As discussed above and in the main text, the cilium beat frequency is sensitive to temperature, i.e., the higher the temperature, the higher the beat frequency. However, the amplitude θ_c^{SD} and curvature $\bar{\kappa}_c$ of all cases were quite stable during extended exposure to ultrasound, a result that is consistent with observations of biciliate wild type cells (Fig. S4). These results show that acoustic trapping had no effect on the ciliary waveform, and the small elevation of ciliary beat frequency was due to device heating induced by the acoustic actuation. Thus, after achieving a steady state temperature, we hypothesize that long-term acoustic trapping has no discernible effect on swimming behavior or waveform shape.
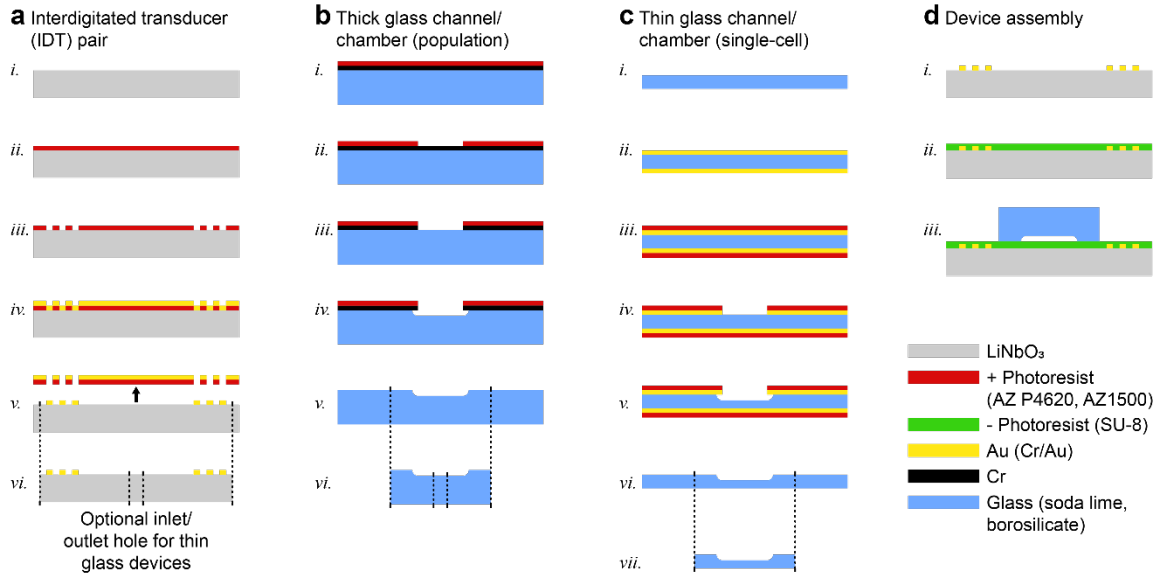
7

Fig. S1. Fabrication of thick- and thin-glass based hybrid BAW/SAW devices. (**a**) Interdigitated transducer (IDT) lift-off process on the piezoelectric LiNbO$_3$ substrate. (**b**) and (**c**) Isotropic etching of channels/chambers in thick- and thin-glass superstrates, respectively. (**d**) Adhesive assembly of a complete device.
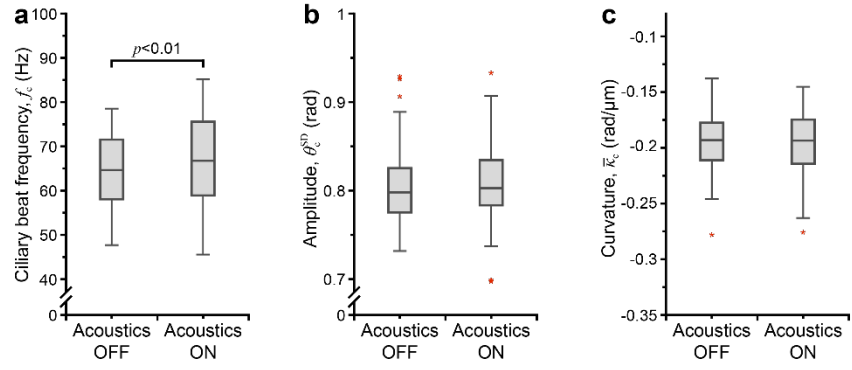
Fig. S2. Effect of ultrasound exposure on cilia beating. (**a**)-(**c**) Measured change in ciliary beat frequency, amplitude, and curvature, respectively, during acoustic actuation of uniciliate *uni1* mutant cells.
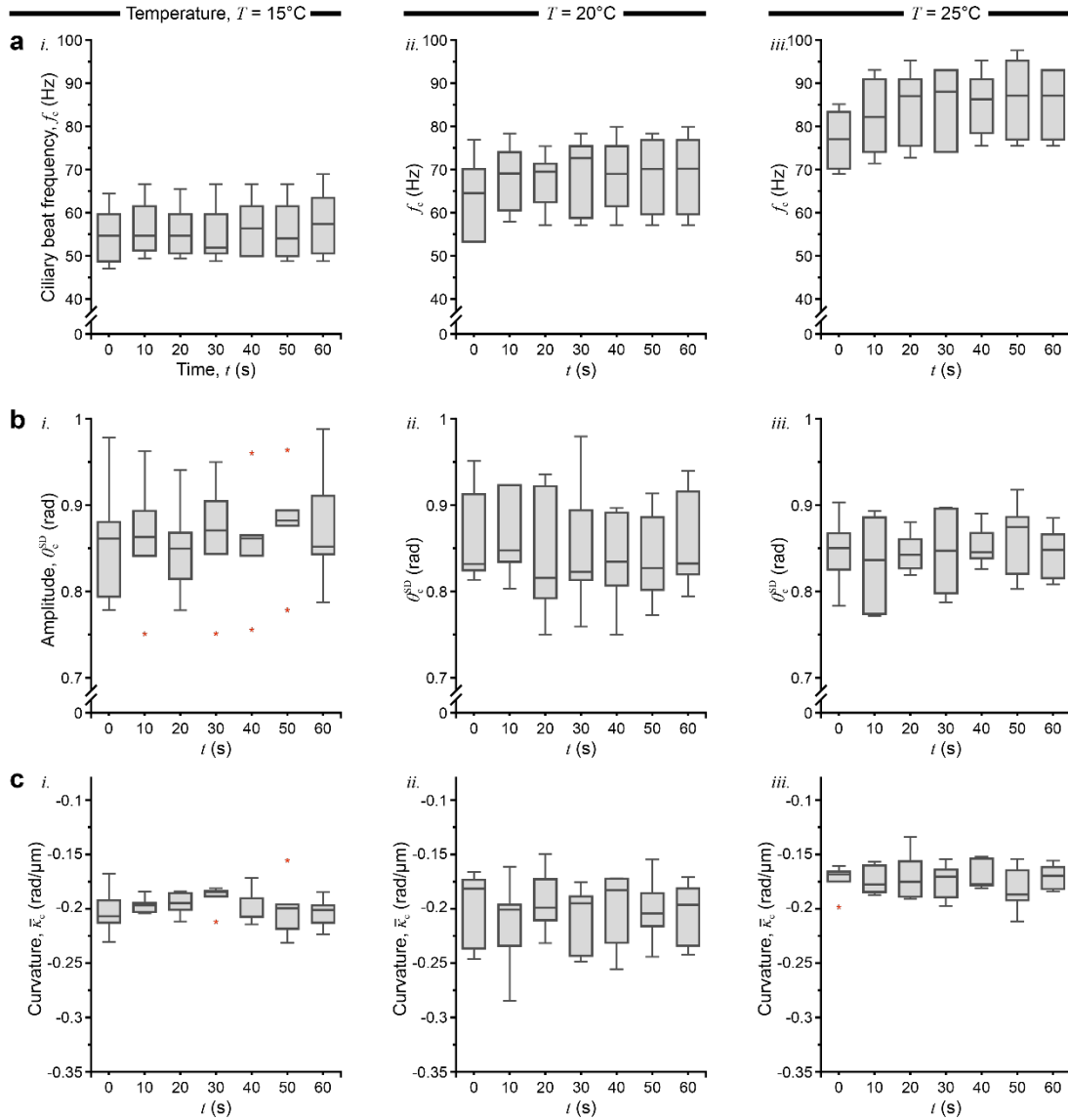
Fig. S3. Effect of long-term acoustic trapping on cilia beating at different temperatures. (**a**)-(**c**) Measured change in ciliary beat frequency, amplitude, and curvature, respectively, during acoustic confinement of uniciliate *uni1* mutant cells for 60 s at three different temperatures (T = 15°C, 20°C, and 25°C).
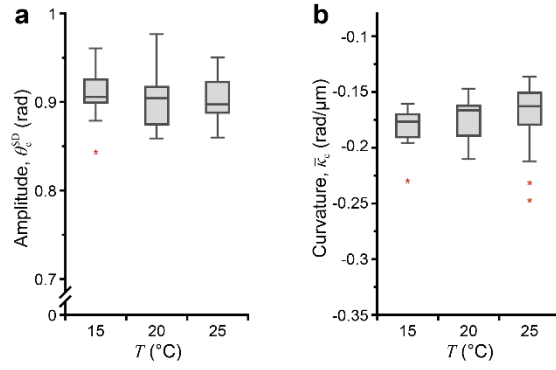
Fig. S4. Effect of increasing temperature on the waveform of the *cis* cilium of biciliate wild type *C. reinhardtii* cells. No significant change in bend amplitude (**a**) or curvature (**b**) is observed as temperature increases from 15°C to 25°C (p>0.05).

Table S1. Symbols used in the main text.

f_{ac}	Acoustic device driving frequency
$\boldsymbol{F}^{\text{rad}}$	Acoustic radiation force
$\boldsymbol{F}^{\text{swim}}$	*C. reinhardtii* swimming force
P_{ac}	Acoustic device drive power
θ_{c}	Cilium angle
$\theta_{\text{c}}^{\text{SD}}$	Cilium bend amplitude
κ_{c}	Cilium bend curvature
$\bar{\kappa}_{\text{c}}$	Spatially averaged cilium bend curvature
f_{c}	Cilium beating frequency
f_{rotation}	*C. reinhardtii* body rotation frequency
η	Fluid viscosity
θ_{b}	Body rotation angle
f_{ref}	Relative frequency of occurrence
$\tilde{\theta}_{\text{c}}$	Normalized cilium beat angle over length

Movie S1 (separate file). Acoustic patterning of a population of *C. reinhardtii* cells to form a stable 6 × 6 grid in an ~545-µm side length square chamber driven at 8.1 MHz.

Movie S2 (separate file). Acoustic patterning of a population of *C. reinhardtii* cells to form a stable pattern of three concentric rings around a central point in an ~545-µm diameter circular chamber driven at 9.8 MHz.

Movie S3 (separate file). Synchronized beating of the *cis* and *trans* cilia of a wild-type biciliate *C. reinhardtii* cell.

Movie S4 (separate file). Asynchronous beating of the *cis* and *trans* cilia of a wild-type biciliate *C. reinhardtii* cell.

Movie S5 (separate file). Three-dimensional (3D) helical rotation of a wild-type biciliate *C. reinhardtii* cell at 15°C.

Movie S6 (separate file). Three-dimensional (3D) helical rotation of a wild-type biciliate *C. reinhardtii* cell at 25°C.

Movie S7 (separate file). Largely synchronized beating of the *cis* and *trans* cilia of a wild-type biciliate *C. reinhardtii* cell at 1 cP viscosity.

Movie S8 (separate file). Asynchronous beating of the *cis* and *trans* cilia of a wild-type biciliate *C. reinhardtii* cell at 8 cP viscosity.

Movie S9 (separate file). Acoustic perturbation of a uniciliate *uni1* mutant cell with enhanced rotation.

SI References

1. L. P. Gor'kov, On the forces acting on a small particle in an acoustical field in an ideal fluid. *Sov. Phys. Dokl.* **6**, 773-775 (1962).
2. R. Barnkob, P. Augustsson, T. Laurell, H. Bruus, Acoustic radiation-and streaming-induced microparticle velocities determined by microparticle image velocimetry in an ultrasound symmetry plane. *Physi. Rev. E* **86**, 056307 (2012).
3. H. Bruus, Acoustofluidics 7: The acoustic radiation force on small particles. *Lab Chip* **12**, 1014-1021 (2012).
4. J. T. Karlsen, H. Bruus, Forces acting on a small particle in an acoustical field in a thermoviscous fluid. *Phys. Rev. E* **92**, 043010 (2015).
5. M. Bottier, K. A. Thomas, S. K. Dutcher, P. V. Bayly, How does cilium length affect beating? *Biophys. J.* **116**, 1292-1304 (2019).
6. P. Bayly *et al.*, Propulsive forces on the flagellum during locomotion of *Chlamydomonas reinhardtii*. *Biophys. J.* **100**, 2716-2725 (2011).
7. P. Bayly, B. Lewis, P. Kemp, R. Pless, S. Dutcher, Efficient spatiotemporal analysis of the flagellar waveform of *Chlamydomonas reinhardtii*. *Cytoskeleton* **67**, 56-69 (2010).
8. J. Gray, G. Hancock, The propulsion of sea-urchin spermatozoa. *J. Exp. Biol.* **32**, 802-814 (1955).
9. R. Johnson, C. Brokaw, Flagellar hydrodynamics. A comparison between resistive-force theory and slender-body theory. *Biophys. J.* **25**, 113-127 (1979).
10. B. M. Friedrich, I. H. Riedel-Kruse, J. Howard, F. Jülicher, High-precision tracking of sperm swimming fine structure provides strong test of resistive force theory. *J. Exp. Biol.* **213**, 1226-1234 (2010).
11. A. T. Chwang, T. Y.-T. Wu, Hydromechanics of low-Reynolds-number flow. Part 2. Singularity method for Stokes flows. *J. Fluid Mech.* **67**, 787-815 (1975).
12. V. Kantsler, J. Dunkel, M. Polin, R. E. Goldstein, Ciliary contact interactions dominate surface scattering of swimming eukaryotes. *Proc. Natl. Acad. Sci. U.S.A.* **110**, 1187-1192 (2013).
13. M. Cui, M. Binkley, H. Shekhani, M. Berezin, J. Meacham, Augmented longitudinal acoustic trap for scalable microparticle enrichment. *Biomicrofluidics* **12**, 034110 (2018).
14. J. A. Holmes, S. K. Dutcher, Cellular asymmetry in *Chlamydomonas reinhardtii*. *J. Cell Sci.* **94**, 273-285 (1989).
15. F. Lux 3rd, S. Dutcher, Genetic interactions at the FLA10 locus: suppressors and synthetic phenotypes that affect the cell cycle and flagellar function in *Chlamydomonas reinhardtii*. *Genet. Med.* **128**, 549-561 (1991).
16. M. Schroda, D. Hemme, T. Muhlhaus, The Chlamydomonas heat stress response. *Plant J.* **82**, 466-480 (2015).
17. B. Xie *et al.*, *Chlamydomonas reinhardtii* thermal tolerance enhancement mediated by a mutualistic interaction with vitamin B 12-producing bacteria. *ISME J.* **7**, 1544-1555 (2013).
18. C. Authesserre *et al.*, Droplet formation of highly viscous Newtonian and non-Newtonian fluids in a microfluidic flow focusing device: scaling of droplet size and production frequency. *TechConnect Briefs* **3**, 198-201 (2016).